Dynamic triggering of shallow earthquakes near Beijing, China

Chunquan Wu,[1] Zhigang Peng,[1] Weijun Wang[2] and Qi-Fu Chen[2]

[1]*School of Earth and Atmospheric Sciences, Georgia Institute of Technology, Atlanta, GA 30332, USA. E-mail: chunquanwu@gatech.edu*
[2]*Institute of Earthquake Science, China Earthquake Administration, Beijing, China*

SUMMARY

We perform a comprehensive analysis of dynamic triggering around the Babaoshan and Huangzhuang-Gaoliying faults near Beijing, China. The triggered earthquakes are identified as impulsive seismic arrivals with clear P and S waves in 5 Hz high-pass-filtered three-component velocity seismograms during the passage of large amplitude body and surface waves of large teleseismic earthquakes. We find that this region was repeatedly triggered by four earthquakes in East Asia, including the 2001 M_w 7.8 Kunlun, 2003 M_w 8.3 Tokachi-oki, 2004 M_w 9.2 Sumatra and 2008 M_w 7.9 Wenchuan earthquakes. In most instances, the microearthquakes coincide with the first few cycles of the Love waves, and more are triggered during the large-amplitude Rayleigh waves. Such an instantaneous triggering by both the Love and Rayleigh waves is similar to recent observations of remotely triggered 'non-volcanic' tremor along major plate-boundary faults, and can be explained by a simple Coulomb failure criterion. We are able to locate five of the earthquakes triggered by the Kunlun and Tokachi-oki earthquakes. These events occurred at shallow depth (<5 km) above the background seismicity near the boundary between NW-striking Babaoshan and Huangzhuang-Gaoliying faults and the Fangshan Pluton. We suggest that these triggered earthquakes occur near the transition between the velocity strengthening and weakening zones in the top few kilometres of the crust, and are likely driven by relatively large dynamic stresses on the order of few tens of KPa.

Key words: Earthquake interaction, forecasting, and prediction; Wave propagation; Dynamics and mechanics of faulting.

GJI Seismology

1 INTRODUCTION

Earthquake interaction has been classified into three categories (Freed 2005): static, quasi-static and dynamic triggering. Static triggering is associated with stress changes from permanent fault displacement, and mostly occurs around the immediate vicinity of the main shock rupture zone. Quasi-static triggering is typically associated with afterslip, viscoelastic relaxation or fluid diffusion and can occur at distances up to a few times the main shock rupture zone. In recent years, many studies have found widespread evidence that large earthquakes could also cause significant increase of seismicity rate in regions that are several hundreds to thousands of kilometres away (e.g. Hill *et al.* 1993; Brodsky *et al.* 2000; Gomberg *et al.* 2001; Hough & Kanamori 2002; Kilb *et al.* 2002; Hough *et al.* 2003; Gomberg *et al.* 2004; Prejean *et al.* 2004; Freed 2005; Hill & Prejean 2007; Velasco *et al.* 2008). This type of triggering is mostly caused by dynamic stresses associated with large amplitude surface waves. Systematic investigations of dynamic triggering could help to improve the understanding of the underlying mechanisms of earthquake initiation and interaction, which are both key components of earthquake forecasting and hazard analysis.

Previously, dynamically triggered earthquakes are identified preferentially near active plate boundary faults or geothermal/volcanic regions with abundant background seismicity (Hill *et al.* 1993; Hill

& Prejean 2007, and reference within). Recent studies have found remotely triggered earthquakes in relatively stable intraplate regions (e.g. Hough *et al.* 2003; Gomberg *et al.* 2004; Velasco *et al.* 2008; Gonzalaz-Huizar & Velasco 2010). Peng *et al.* (2010b) found clearly triggered earthquakes in north China after the 2008 M_w 7.9 Wenchuan earthquake. Jiang *et al.* (2010) extended the analysis of Peng *et al.* (2010b) to the rest of continental China, and found many triggered earthquakes near active faults in different tectonic settings. These observations further support the view that earthquake dynamic triggering is a ubiquitous phenomenon that is independent of tectonic environments, and a number of physical mechanisms could play a role in dynamic triggering (Velasco *et al.* 2008). However, the underlying mechanisms of dynamic triggering in various tectonic environments remain a topic that need further investigations (Hill & Prejean 2007).

Physical models proposed to explain the dynamic triggering process typically fall into two categories (Hill & Prejean 2007; Hill 2008): direct triggering by friction failure via different modes (e.g. Gomberg *et al.* 1997, 2001, 2005; Perfettini *et al.* 2003; Johnson & Jia 2005; Hill 2008), or indirect triggering through excitation of crustal fluids and/or transient deformation (e.g. Brodsky *et al.* 1998, 2000, 2003; Linde & Sacks 1998; Hill *et al.* 2002). The friction failure model assumes that the critically stressed faults are triggered by the transient dynamic stress from the passing seismic waves, so

the triggered seismicity usually occurs during or immediately after the teleseismic waves. On the other hand, indirect triggering models generally involve some time delays between the passing seismic waves and the onset of triggered earthquakes, due to the response time of fluids or transient deformation.

Many factors could play a role in determining the triggering potential at each site. These includes dynamic stresses at the triggering depth (wave type, amplitude, frequency and incidence angle), local conditions (triggered fault type, fault orientation, tectonic environments and hydrological properties) and information about the triggered earthquakes (origin times, hypocentral locations and focal mechanisms). Comprehensive investigation of these parameters would not only help to better constrain the physical mechanisms of dynamic triggering, but also help to identify the conditions that favour dynamic triggering at various tectonic settings.

Here we present a systematic analysis of dynamic triggering near Beijing in north China associated with four large teleseismic earthquakes in East Asia (Fig. 1). We focus on this region because it is covered by a dense regional seismic network, and previous studies have identified remotely triggered seismicity by the 2008 M_w 7.9 Wenchuan earthquake (Peng *et al.* 2010b; Jiang *et al.* 2010). Following our previous study, we find that this region was also triggered by four large teleseismic earthquakes (including the Wenchuan earthquake). The local earthquakes are likely triggered by Coulomb stress changes at shallow depths (<5 km), and the possible controlling parameters for dynamic triggering include amplitude, incident angle, and type of the surface waves.

2 STUDY REGION AND DATA

2.1 Study region

Our study region is about 35 km southwest of Beijing, and it is within the southwestern part of the North China Plain (Fig. 1). This region is along the major block boundary of the Taihang Mountain in the west and the Bohai Bay Basin in the east, and there is a significant lateral thickness variation of lithosphere at this region (Chen *et al.* 2008). This region is also characterized by many normal faults and compressive folds in the NW–NWW directions (Deng *et al.* 2003), including the Babaoshan and Huangzhuang-Gaoliying faults, and several other major parallel faults (Fig. 1). In particular, the Babaoshan and Huangzhuang-Gaoliying faults are both normal faults with the strike in the NW direction. The dipping angles of Babaoshan and Huangzhuang-Gaoliying faults are 25–35° and 65–75°, respectively (Che *et al.* 1997). Previous studies of leveling, gravity, geomagnetic and strain field of region close to these faults suggest that the shallow part of Babaoshan fault is currently creeping, while the Huangzhuang-Gaoliying fault is currently locked (e.g. Che *et al.* 1997; Che & Fan 2003). The background seismicity in this region is relatively low, and the earthquakes are generally not close to the faults inferred from the surface trace and dipping angles. Another interesting feature in the study region is the Fangshan Pluton, which is an intrusive Mesozoic pluton (133–128 Ma) at the junction of Taihang tectonic belt and Yanshan intraplate orogenic belt (Yan *et al.* 2006; Wang *et al.* 2011). The intrusion is mainly composed of quartz diorite and granodiorite, and its lithological boundary to the host rocks is marked as a curve around stations NKY and ZKD in Fig. 1. This region has been seismically active in historic times, with several M 6–7 earthquakes occurring in the 17–18th century (e.g. an $M \sim 6$ earthquake on 1658 February 03 and an $M \sim 6.5$ on 1730 September 30). Currently the region is seismically quiet,

with $\sim$23 $M > 1$ earthquakes each year since 2000 (Peng *et al.* 2010b).

2.2. Seismic data

The analysis employs seismic data recorded by 45 stations in the Capital-Circle (CC) digital seismograph network (Fig. 1) operated by the China Earthquake Networks Center (Liu *et al.* 2003; Chen *et al.* 2006). The network consists of 107 broadband, borehole and surface short-period stations. First we search the Advanced National Seismic System (ANSS) catalogue for all the $M \geq 7.5$ teleseismic earthquakes since 2000 with hypocentral depth less than 100 km, and download the seismic data from 8 hr before until 8 hr after each teleseismic earthquake recorded at the broadband station BJT that belongs to the New China Digital Seismograph Network (IC). We visually examine the 5 Hz high-pass filtered seismograms of all the 39 teleseismic earthquakes, and identify clear impulsive signals with double peaks during the passage of surface waves of four large earthquakes in East Asia, including 2001 M_w 7.8 Kunlun, 2003 M_w 8.3 Tokachi-oki, 2004 M_w 9.2 Sumatra and 2008 M_w 7.9 Wenchuan earthquakes (Table 1). Fig. 2 shows that the peak ground velocities (PGVs) measured from both the vertical and transverse components for the four earthquakes are generally larger than those for the rest of the earthquakes. We note that other four teleseismic earthquakes (e.g. 2001 M_w 7.7 El Salvador, 2001 M_w 7.7 India, 2006 M_w 8.3 Kuril and 2007 M_w 8.1 Solomon earthquakes) are also associated with some local high-frequency signals during their passing surface waves, but the signals are not clear as the previous four cases, and the other 31 teleseismic earthquakes show no sign of triggered earthquakes (Table S1). Hence, in this study we focus on those four earthquakes with clear triggering and request the data from all stations in the CC network.

3. ANALYSIS PROCEDURE

The analysis procedure generally follows that of (Peng *et al.* 2010b; Jiang *et al.* 2010) and is briefly described here. We visually examine all the records, and remove those bad traces with incomplete surface wave recording, because triggered seismicity is generally found during and immediately after the large amplitude surface waves (Velasco *et al.* 2008). After the selection process, we obtain a total of 154 station-event pairs for subsequent analysis. We remove the instrument response to obtain the velocity records. We also remove the mean and trend, and apply a 5 Hz two-way high-pass Butterworth filter to all the data. Then we visually identify local earthquakes as impulsive seismic energies with clear P and S waves on the 5 Hz high-pass-filtered three-component velocity records (e.g. Fig. 3d). In the following analysis, we focus only on the station-event pairs with at least one identified local earthquake within 1-hr of the P arrivals of the teleseismic earthquakes.

In addition to visual inspection, we also compare the seismicity rate before and after the P arrival time of each teleseismic earthquake based on handpicked local earthquakes with clear double picks, and evaluate the significance of seismicity rate changes by computing the β-statistic value. The β-statistic measures the differences between the observed number of local earthquakes after the main shock and the expected number from the average seismicity rate before the main shock, and scaled by the standard deviation of the seismicity rate (Matthews & Reasenberg 1988; Reasenberg & Simpson 1992). The detailed procedures to compute the β statistic values are described in Appendix A.
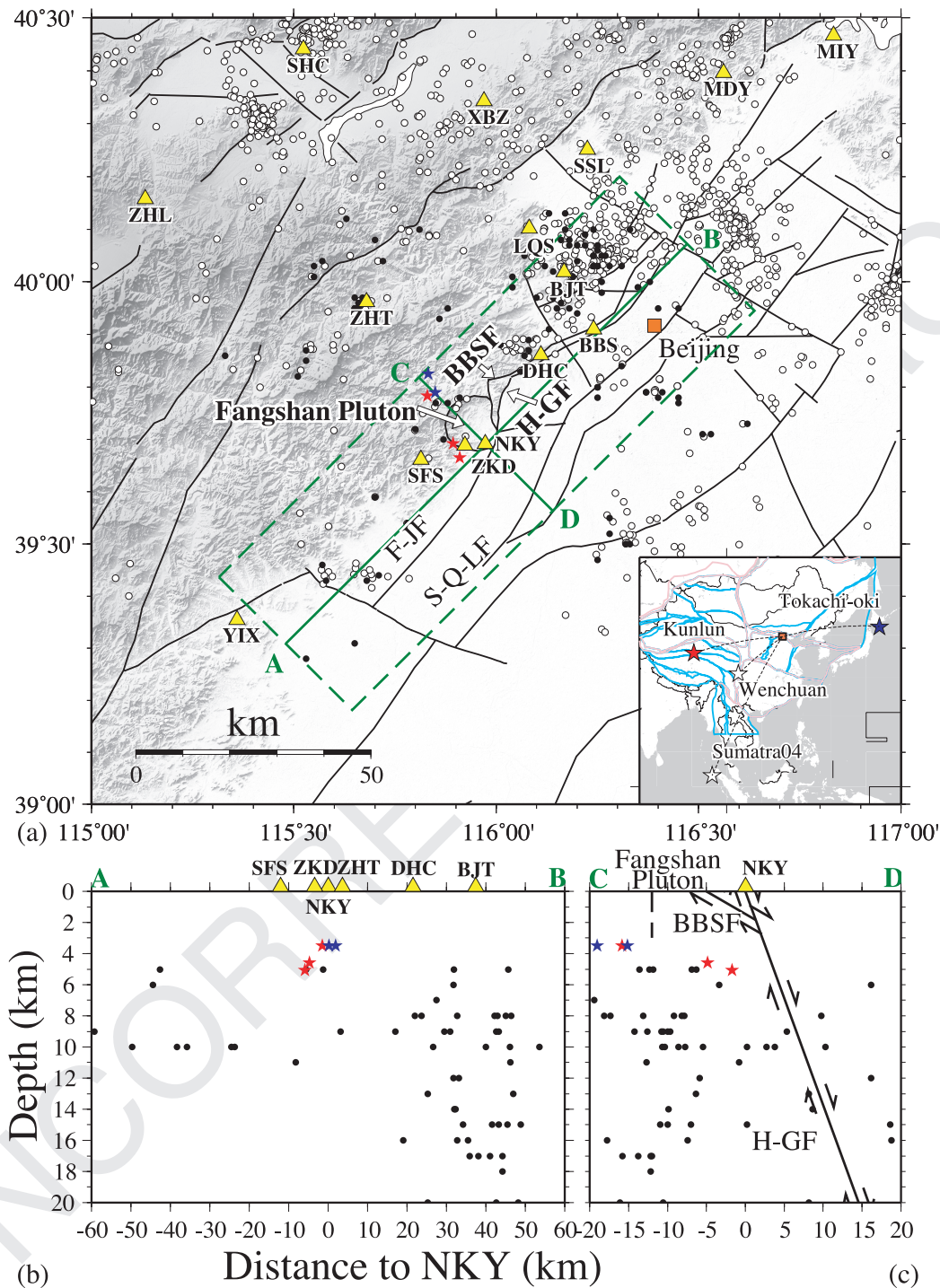
COLOUR

Figure 1. (a) A map showing the study region around Beijing in north China. The yellow triangles mark the seismic stations in the CC network utilized in this study. Red and blue stars mark the epicentres of local earthquakes triggered by the 2001 M_w 7.8 Kunlun and 2003 M_w 8.3 Tokachi-oki earthquakes, respectively. The filled and open circles mark the background seismicity with waveforms and listed in the local catalogue, respectively. The regional and local faults are marked as black lines. The Babaoshan fault, Huangzhuang-Gaoliying fault, Fangshan-Jumahe Fault, Shunyi-Qianmen-Liangxiang Fault, and Fangshan Pluton are labelled as BBSF, H-GF, F-JF, S-Q-LF and Fangshan Pluton, respectively. The solid green line along AB and the green dashed line box show the projection line and projection area in (b). The orange square shows the location of Beijing. The inset shows a map of China with the box corresponds to the study region. The red and blue stars mark the epicentres of the 2001 M_w 7.8 Kunlun and 2003 M_w 8.3 Tokachi-oki earthquakes, respectively. The open stars show the epicentres of the 2004 M_w 9.2 Sumatra and the 2008 M_w 7.9 Wenchuan earthquakes. The dashed lines show the ray paths. The major tectonic block boundaries and block-boundary faults are shown in pink and cyan lines, respectively. (b) Cross-section view of the line AB in (a). The triggered and background seismicity within the green box in (a) and nearby stations are projected the line AB. (c) Cross-section view of the line CD in (a). The triggered and background seismicity within the green box in (a) and the station NKY are projected to the line CD. The black lines show the schematic dipping directions of Babaoshan and Huangzhuang-Gaoliying faults, with arrows showing the slip directions. The vertical dashed line shows the surface boundary of the Fangshan Pluton.

Table 1. List of the information for all the four large teleseismic events in East Asia that clearly triggered local earthquakes in our study region.

| Event name	Year	Month	Days	Hours	Minutes	Seconds	Longitude (km)	Latitude (km)	Depth (km)	Magnitude (M_w)	Distance to NKY (km)	Backazimuth (°)
Kunlun	2001	11	14	09	26	10.0100	90.54101	35.94600	10.0000	7.80	2269.5601	267.5027
Tokachi-oki	2003	09	25	19	50	6.3600	143.91000	41.81500	27.0000	8.30	2360.9893	75.2148
Sumatra	2004	12	26	00	58	53.4500	95.98200	3.29500	30.0000	9.20	4507.7031	211.6947
Wenchuan	2008	05	12	06	28	1.5700	103.32201	31.00200	19.0000	7.90	1497.6155	233.8280
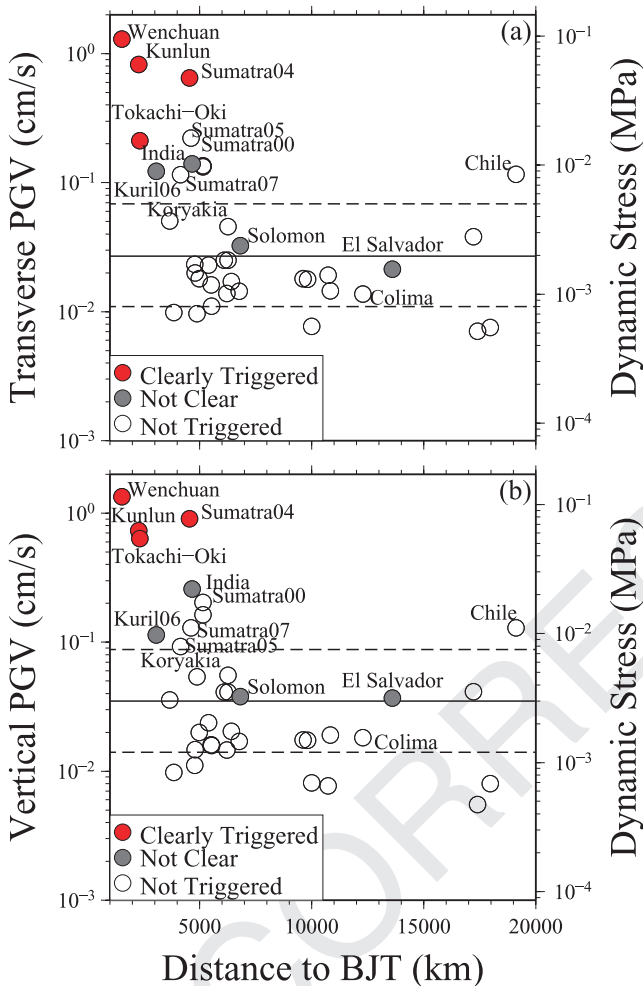
Figure 2. (a) Transverse peak ground velocity (PGV) and the corresponding dynamic stress (DS) plotted against epicentral distance at station BJT for all the 39 teleseismic events utilized in the preliminary survey. The *y*-axes on the left and right show the scales for the PGV and DS, respectively. The DS is estimated using the relationship $DS = G * PGV/V$ (Hill *et al.* 1993), where V is the phase velocity, and assumed to be 3.5 km s^{-1}, and G is the shear rigidity, which is assigned as a nominal value of 30 GPa. Solid red and grey circles mark the teleseismic events with clear and possible triggering, respectively. Open circles mark the teleseismic events without triggering. The horizontal solid and dashed lines mark the approximate threshold and range of PGV for dynamic triggering, respectively. (b) Similar plot as (a) for vertical PGV and DS.

4. RESULTS

4.1 General patterns

After visual inspection of the 5 Hz high-pass filtered data from all the CC network stations, we identified 19 triggered earthquakes the first hour following the *P* arrivals of the four teleseismic

earthquakes (Table S2, Figs 3–6). Fig. 3 shows seismic activity ±30 d of the Kunlun earthquake from regional earthquake catalogue (Fig. 3a) and the high-pass-filtered envelope function at station NKY (Fig. 3b). Similar examples for the station-event pairs NKY-Tokachi-oki, ZHT-Sumatra2004, NKY-Wenchuan are shown in Figs 4–6. We note that none of the visually identified local earthquakes from the high-pass filtered continuous data are listed in the earthquake catalogue, and there is no clear change in seismicity rate from the catalogue ±30 d of the four teleseismic earthquakes we analysed. In comparison, we do see significant increase of seismicity rate ($\beta > 2$) from the continuous recordings. This is consistent with recent observations of dynamic triggering in other regions (e.g. Gomberg *et al.* 2004; Prejean *et al.* 2004; Jiang *et al.* 2010), and suggests that analysing continuous seismic data is more effective in identifying remotely triggered earthquakes (Hill & Prejean 2007). Because of this, we focus on the results from the continuous waveform data in the following section.

Overall the surface waves of the four analysed teleseismic earthquakes coincide with locally triggered earthquakes in our study region, and the increase of seismicity rate is statistically significant ($\beta > 2$; Figs 3–6). In all four cases, the triggered seismic events occur during the first few cycles of the Love waves, and occurred again during the large-amplitude Rayleigh waves (Fig. 7). The amplitudes of the triggered earthquakes during the Love waves appear to be larger than during the Rayleigh waves for the Kunlun, Sumatra and Wenchuan earthquakes (Figs 3, 5–7). For the Tokachi-oki earthquake, the triggered earthquakes during the Rayleigh waves have much larger amplitudes (Fig. 4).

4.2 Locations of the triggered earthquakes

From visual comparison of the arrival times of the triggered earthquakes, we find five triggered earthquakes that are recorded by at least three stations. An example of high-pass-filtered seismograms showing triggered earthquakes recorded at different stations is given in Fig. 8. Next, we pick the *P*- and *S*-arrival times for each station-event pair, and locate the five local earthquakes in both HYPO2000 and HYPO71 programs (Klein 2002) using the hand-picked *P*- and *S*-arrival times. The obtained locations from both methods are nearly identical. We also use the double-difference relocation program HypoDD (Waldhauser 2001) to relocate the five triggered earthquakes together with the background seismicity (a total of 107 earthquakes from 2001 to 2007) based on both the hand-picked and waveform cross-correlated travel times. Because the relocation method mostly works for earthquakes that are in close distance, the relocation process does not change the locations of the five triggered earthquakes that are relatively far from most of the background earthquakes (Fig. 1).

As shown in Fig. 1, the five triggered earthquakes are very close to the station NKY (<20 km), and appear to be at shallow depth (<5 km, Table S2), just above the depth range of the background seismicity. We also find that the handpicked *S*–*P* times at
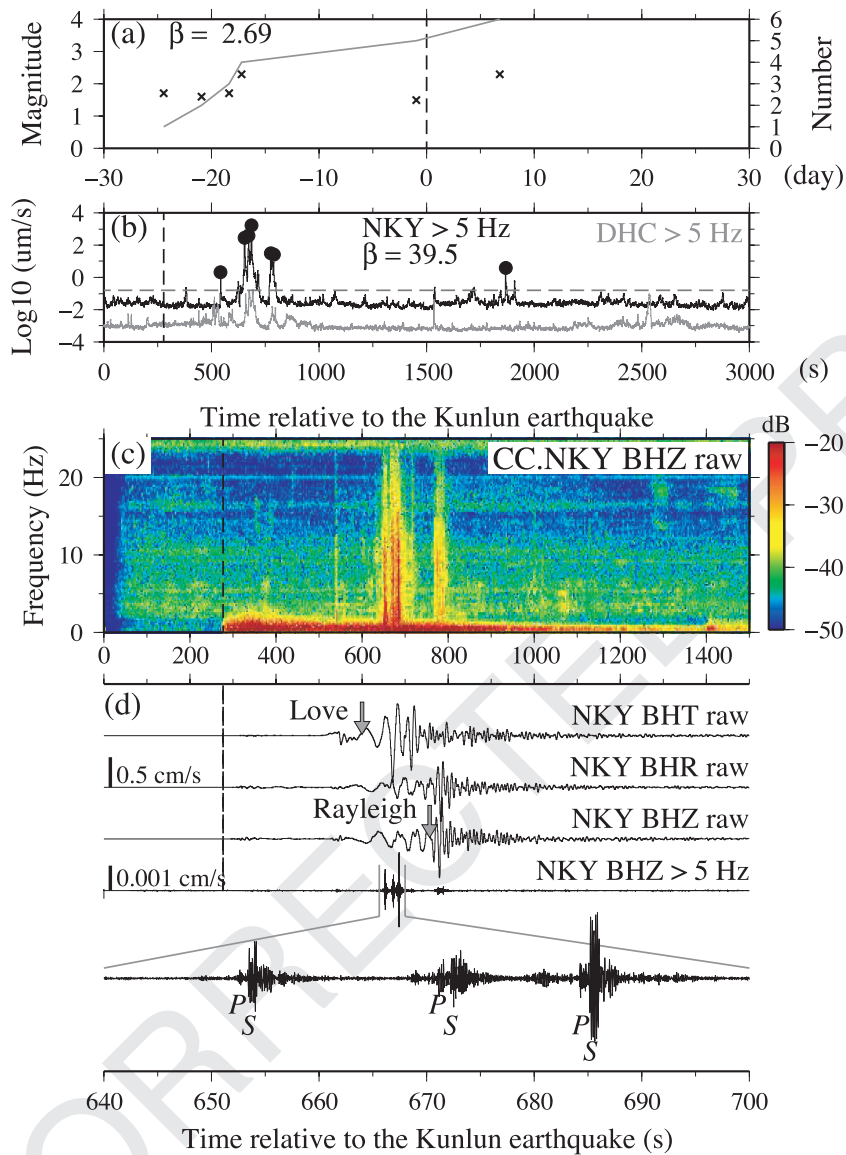
Figure 3. (a) Seismicity ±30 d of the Kunlun main shock and within 120 km of station NKY near Beijing. The crosses mark the events listed in the regional earthquake catalogue and the line shows the cumulative number of events. The corresponding β-statistic value based on the catalogue is 2.69. The vertical dotted line marks the *P*-arrival time of Kunlun earthquake at NKY through panel (a)–(d). (b) The 5-Hz high-pass-filtered envelope functions at station NKY (solid line) and the nearby station DHC (grey line) within ~3000 s of the *P*-wave arrival of the Kunlun earthquake (vertical dashed line). The solid circles mark the hand-picked events after the *P* arrival. The corresponding β statistic value is 39.5. The horizontal dashed line marks the 10 times median absolute deviation (MAD) threshold. (c) The spectrogram of the vertical component seismogram recorded at station NKY. We applied a 0.5 Hz high-pass filtering to the raw data before computing the spectrogram to remove the potential high frequency artefact by computing short-time FFT for long-period signals (Peng *et al.* 2011). The colour bar shows the spectra value in $10\log_{10}$ (cm s^{-1} Hz^{-1}) dB. (d) Raw and high-pass-filtered seismograms showing the teleseismic waves of the Kunlun earthquake and local seismic events, respectively. The top three traces: the raw three component (transverse, radial and vertical) seismograms recorded at station NKY. The grey arrows indicate the predicted Love and Rayleigh wave arrival times based on the peaks in seismogram assuming Love wave velocity of 3.8 km s^{-1}, and Rayleigh wave velocity of 3 km s^{-1}. The middle trace: 5 Hz high-pass-filtered seismograms on vertical component showing small local earthquakes during and immediately after the passage of surface waves. The bottom trace: a zoom-in plot of the vertical seismograms showing the *P* and *S* waves of the three triggered earthquakes recorded at station NKY.

station NKY for the triggered earthquakes are generally less than those for the background earthquakes (Fig. 9), further suggesting that the triggered earthquakes are shallower or closer to the station NKY than the background earthquakes. The epicentral locations of these triggered earthquakes are near the boundaries of the Babaoshan/Huangzhang-Gaoliying faults and the Fangshan Pluton (Fig. 1). Because the subsurface structures beneath this region are still not clear at this stage, we do not know whether the triggered earthquakes occur on the shallow portion of the normal faults, or on the boundary faults around the Fangshan Pluton.

We estimate the local magnitude M_L of the triggered earthquakes to be in the range of –0.5 to 2.4 (Table S2), based on the peak amplitude averaged over two horizontal components and the *S–P* times (Liang *et al.* 2008; Peng *et al.* 2010b). Because we obtain the peak amplitude using 5 Hz high-pass filtered data, the magnitudes computed here are likely to a lower bound estimate, but we do not make any magnitude corrections in this study.
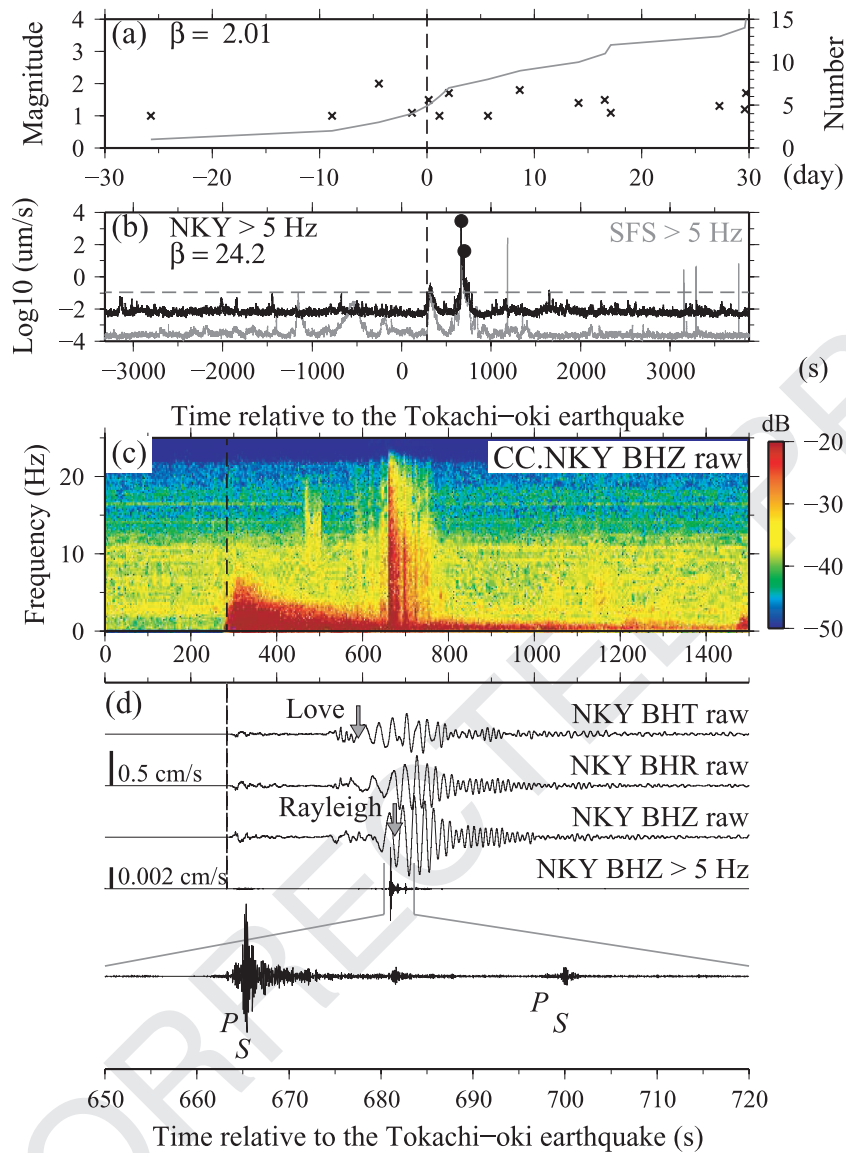
Figure 4. Similar plot as Figure 3 for the station-event pair NKY and the 2003 Tokachi-oki earthquake.

To examine whether the triggered earthquakes are regular or low-frequency earthquakes (e.g. Shelly *et al.* 2006) in the shallow crust, we compare the stacked spectra of 15 triggered earthquakes with the spectra of 18 nearby background earthquakes within 30 km of the station NKY (Fig. 10). We use a 15 s time window starting 5 s before the handpicked *P*-arrivals to compute the spectra, and smooth the spectra with a moving window of five points. Due to the lack of accurate site response and attenuation for the medium, and the contamination of spectra in the lower frequency range (<8 Hz) by the passage of teleseismic surface waves, we do not attempt to correct for the path and site effects and fit the source spectra. Alternatively, we shift the spectra to the same level so that we are able to compare the frequency content of the triggered vs. background events. We find that the spectra for triggered earthquakes show slightly faster decay rate in the frequency range of 10–20 Hz than those for background earthquakes (Fig. 10b), suggesting that the triggered events may have lower corner frequencies than the background events However, because we did not correct for the path and site effects, the difference in the source spectra is not conclusive.

5 MODELLING

To better explain our observations, we model the dynamic stress caused by the passage of Rayleigh and Love waves with an arbitrary incident angle on critically stressed faults under the Coulomb failure criteria. The modelling procedure generally follows that of Hill (2008) and Gonzalaz-Huizar & Velasco (2010) and is briefly described in Appendix B. Here we assume that those triggered earthquakes occur on or close to the NW-striking Babaoshan or Huangzhuang-Gaoliying faults with different dipping angles. The modelling results indicate that for the surface waves incident on a normal fault plane striking at NW direction, and dipping at 30° or 70° (Fig. 1), the triggering potential of the Love wave is largest for teleseismic earthquakes with incidence angle around −135°, −45°, 45° or 135°. The triggering potential of the Rayleigh wave is the highest for teleseismic earthquakes with incidence angle around −90° or 90° (Fig. 11). We test our model using the dipping angles of the Babaoshan and Huangzhuang-Gaoliying faults (30° and 70°, see Fig. 1c), combined with the coefficient of friction μ in the range of 0.2–0.6, and this does not change the overall shape of the triggering
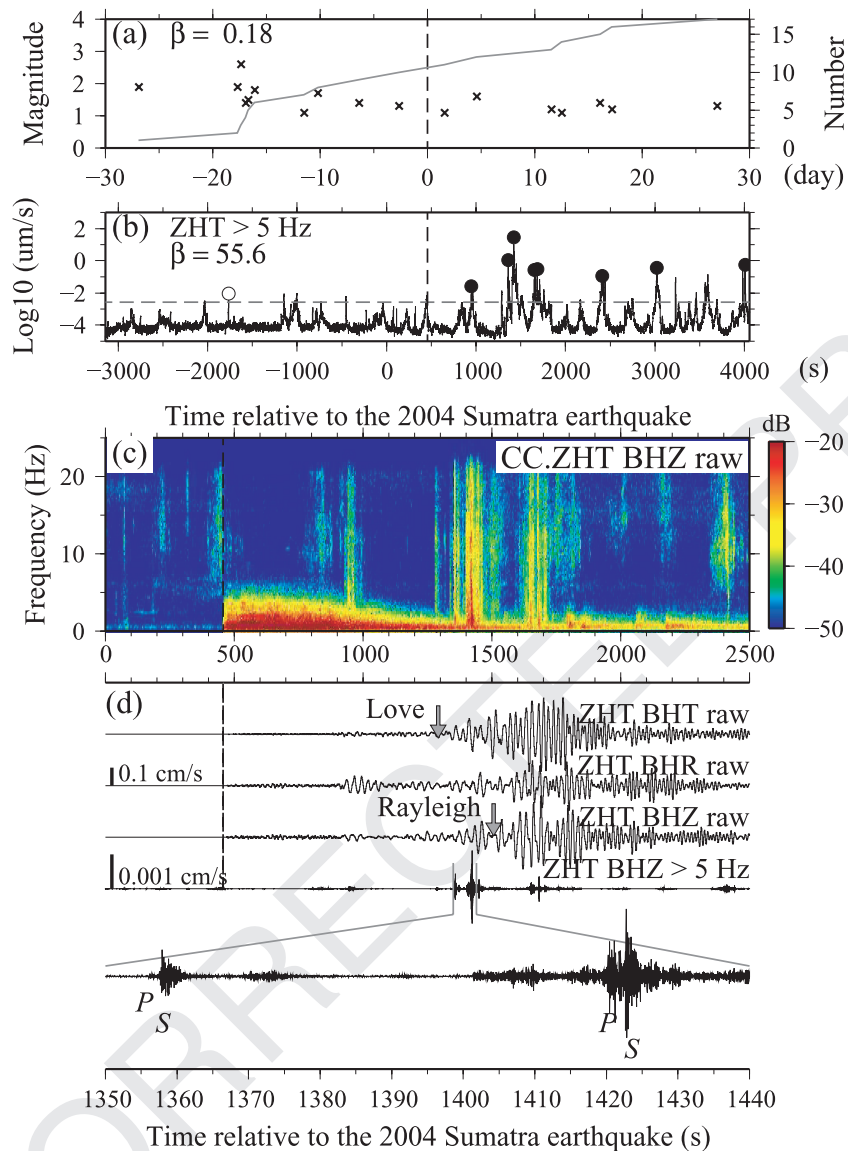
Figure 5. Similar plot as Figure 3 for the station-event pair ZHT and the 2004 Sumatra earthquake. In panel (b), the open and solid circles mark the hand-picked events before and after the *P* arrival, respectively.

potentials (Fig. 11). Our modelling results suggest that, based on the friction failure model, the triggering potentials for the Love and Rayleigh waves differ for different incident angles. Because the incidence angles for the four $M_w > 7.8$ earthquakes used in this study span a range of only $-15°$ to $45°$, the available data do not allow a thorough test for our modelling results as shown in Fig. 11.

6 DISCUSSIONS

Our previous studies have identified clear triggering in continental China following the 2008 Wenchuan earthquake (Peng *et al.* 2010b; Jiang *et al.* 2010). This study provides additional evidence of dynamic triggering within intraplate regions near Beijing. We found that this region is repeatedly triggered by at least four large teleseismic earthquakes. This is consistent with recent observations in other intraplate regions (e.g. Gomberg *et al.* 2004; Velasco *et al.* 2008), and further suggests that dynamic triggering can occur in a wide range of tectonic environments. In addition, identification

of multiple triggering cases at a specific site provides a unique chance to investigate the physical models and necessary conditions for dynamic triggering in intraplate regions.

As mentioned before, the physical models proposed to explain remotely triggered seismology are generally associated with frictional failure and/or excitation of crustal fluids/transient deformation (e.g. Hill & Prejean 2007). We note that the triggered earthquakes occurred during the first few cycles of the Love waves, and occurred again during the large amplitude Rayleigh waves (Figs 3–7). Recent studies of dynamically triggered earthquakes and tremors suggest that Rayleigh wave triggering could be explained by both Coulomb failure and fluid excitation, while Love wave triggering is more likely via Coulomb failure, because Love wave particle motions involve pure-shear strain with no volumetric component to excite fluid movements (Rubinstein *et al.* 2007, 2009; Miyazawa *et al.* 2008; Peng & Chao 2008; Hill 2008; Peng *et al.* 2008, 2009, 2010a). In addition, most of the triggered earthquakes identified in this study are in phase with the passing surface waves without clear time delays (Fig. 7), so they are better explained by the Coulomb failure crite-
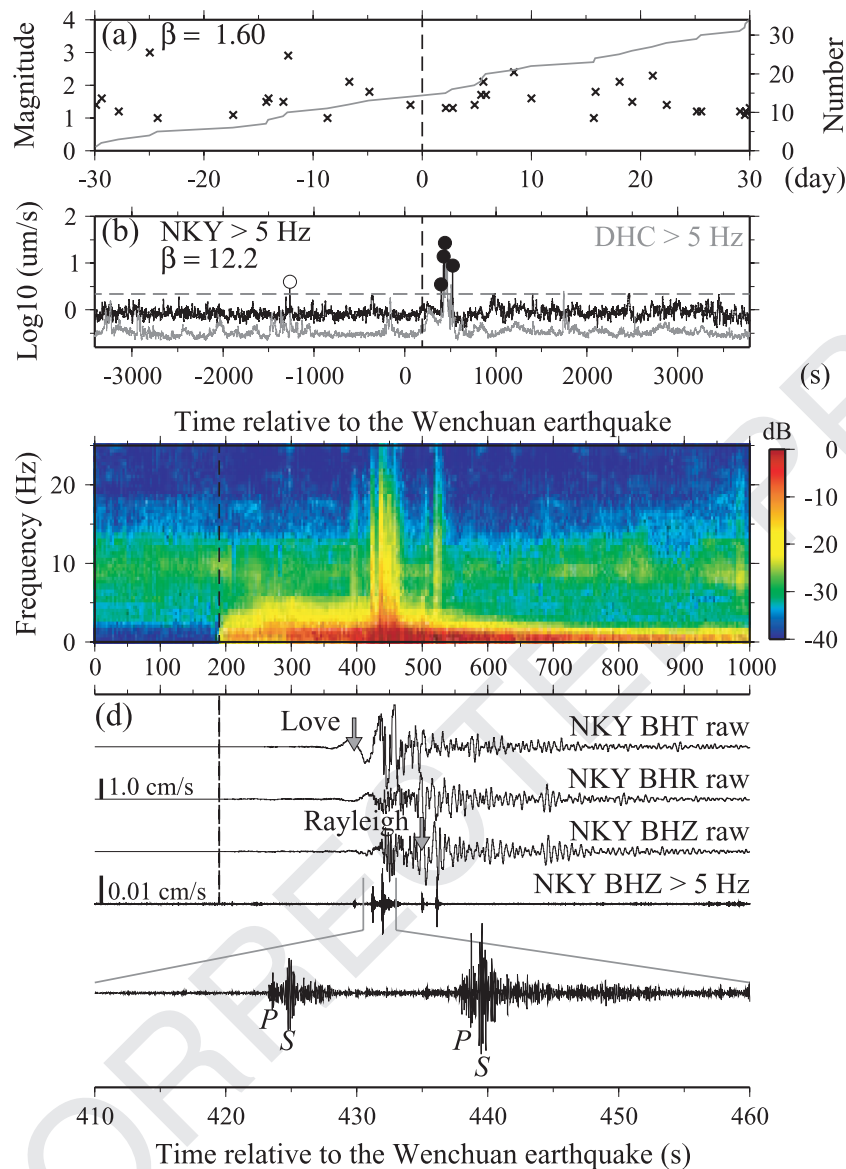
Figure 6. Similar plot as Figure 3 for the station-event pair NKY and the 2008 Wenchuan earthquake, modified from Jiang *et al.* (2010). In panel b, the open and solid circles mark the hand-picked events before and after the *P* arrival, respectively.

ria (Hill 2008, 2010; Gonzalaz-Huizar & Velasco 2010). However, we only examine the continuous data within several hours after the *P*-arrival of each teleseismic earthquake due to the availability of continuous recording, so additional triggered earthquakes at later times associated with fluids or long-term aseismic creep (e.g. Prejean *et al.* 2004; Johnston *et al.* 2004) could escape our detection in this study.

The aforementioned friction failure model generally assumes that the passage of seismic waves change the stress within the critically stressed local faults and trigger failure dynamically. Typically the effect of the passing seismic waves is quantified by the peak dynamic stress (PDS), which can be approximated from the PGV in a velocity seismogram (Hill *et al.* 1993). We examined PGV and PDS of the four teleseismic earthquakes recorded at NKY, the closest station to the epicentres of the triggered earthquakes, and we found that the vertical PGVs of the Kunlun, Tokachi-oki, 2004 Sumatra and Wenchuan earthquakes are 0.69, 0.59, 0.91, 1.27 cm s^{-1}, respectively. These PGVs would correspond to the PDSs in the range

of 60–130 kPa, well above the triggering thresholds found at other regions (Brodsky & Prejean 2005; Peng *et al.* 2009; Van der Elst & Brodsky 2010). This is likely because the only available station during the entire study period is IC.BJT, which is about 50 km away from most of the triggered earthquakes around station NKY. Hence, we can only identify the most clear triggering case with large PGVs and PDSs. In addition, the PGVs of the four analysed teleseismic earthquakes at station IC.BJT are generally higher than other events, mostly because of their large magnitudes ($\sim M_{\rm w} >$ 7.8) and relatively short propagation distances (Fig. 2). This observation indicates that input wave amplitude plays an important role in controlling the triggering potential and the resulting amplitudes of the triggered events (Peng *et al.* 2009; Rubinstein *et al.* 2009; Chao *et al.* 2011).

In addition to the wave amplitude, other factors affecting the dynamic stress acting on the fault plane include the hypocentral depth, fault orientation, incident angle and type of seismic waves (Gonzalaz-Huizar & Velasco 2010; Hill 2010). Our modelling
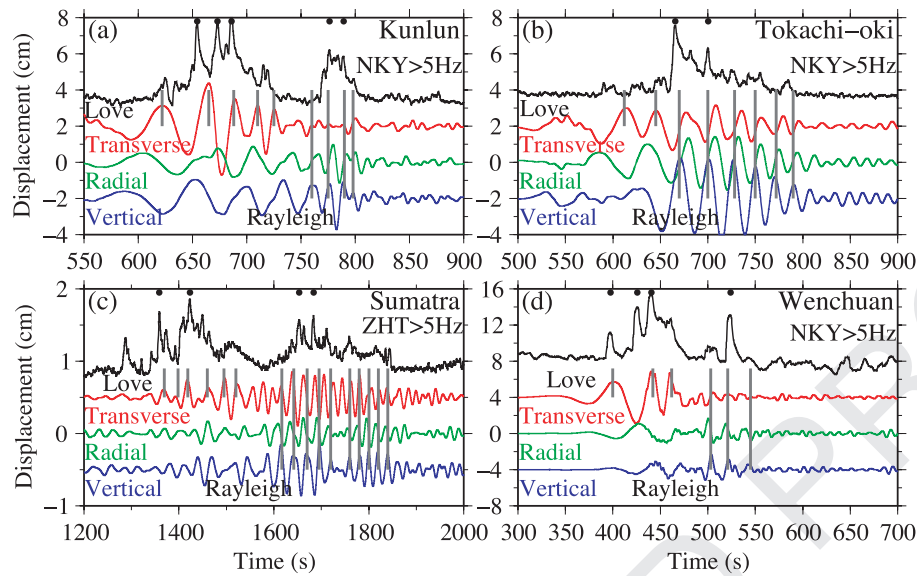
Figure 7. Zoom-in plots of the timing between the triggered seismicity and surface waves. (a) The top black trace shows the smoothed envelope function in logarithmic scale averaged from the 5 Hz high-pass filtered three-component velocity records at NKY for the 2001 Kunlun earthquake. The broadband transverse, radial, and vertical displacement seismograms are plotted as red, green and blue colours, respectively. The black dots on the top mark the timing of the triggered events. The short and long vertical grey lines mark the peaks of Love and Rayleigh waves, respectively. Plots (b), (c) and (d) are similar plot as (a) for the 2003 Tokachi-oki, 2004 Sumatra, and 2008 Wenchuan earthquakes, respectively.
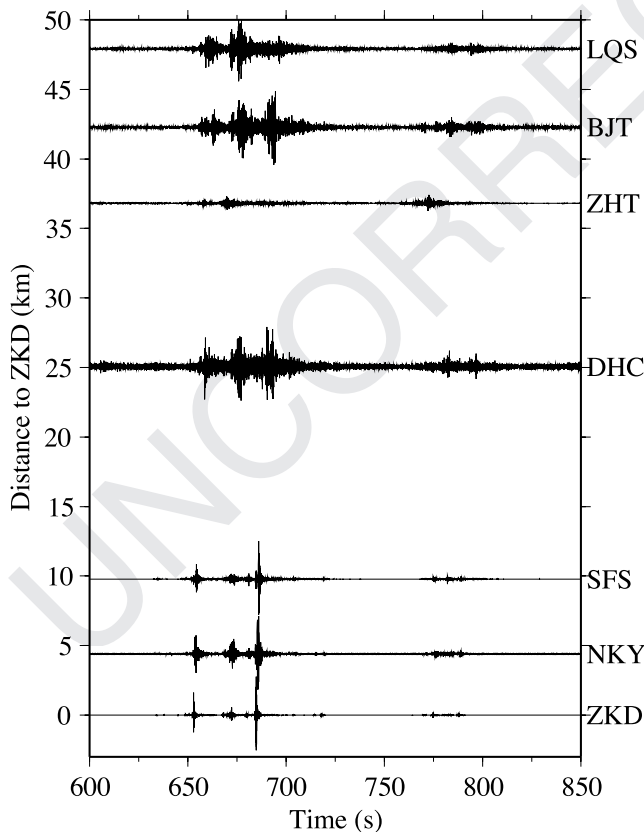

Figure 8. 5 Hz high-pass-filtered seismograms aligned by the distance from the station ZKD during the surface waves of the Kunlun earthquake. Zero time is the Kunlun earthquake origin time.

results show that the triggering potential for the Love wave is larger than that for the Rayleigh wave for incidence angles ±45° on normal faults at depths of ∼4km with dips of 30° and 70° (Fig. 11). This is consistent with the observations that for the 2001 Kunlun, 2004 Sumatra and 2008 Wenchuan earthquakes, the locally triggered earthquakes during the Love wave generally have larger amplitudes than the local earthquakes during Rayleigh wave. For the 2003 Tokachi-oki earthquake, the triggered earthquakes during the Rayleigh wave have larger amplitudes than during the Love wave. This could be explained by the fact that the Rayleigh wave amplitude is above three times the Love wave amplitude, while our simple modelling analysis assumes equal surface displacement amplitudes for both the Love and Rayleigh waves. We note that the incident angles of the surface waves for the 2004 Sumatra and 2008 Wenchuan earthquakes are in the range of relatively lower triggering potentials for both Love and Rayleigh waves (−15° to 15°, see Fig. 11). However, we still observe clear dynamic triggering for the two wave types (Figs 4 and 6). This is probably due to the fact that the PGVs at our study region for both Sumatra and Wenchuan earthquakes are higher than other teleseismic events (Table S1). As mentioned before, the observations and modelling results are somewhat limited by the small number of available teleseismic events and the relatively simple modelling, and the PGVs and other factors in dynamic triggering are still not clear at this point. Systematic studies of a larger dataset and detailed waveform modelling would be helpful to better constrain the physical models of remote triggering in this and other tectonic environments.

The five triggered earthquakes with hypocentral locations all occurred at shallow depth (<5 km), above the depth range of background seismicity (Fig. 1b). One potential cause of shallow depth could be the reduction of seismic velocity in the shallow crust during the passage of large-amplitude surface waves. However, the reductions of seismic velocities are generally on the order of
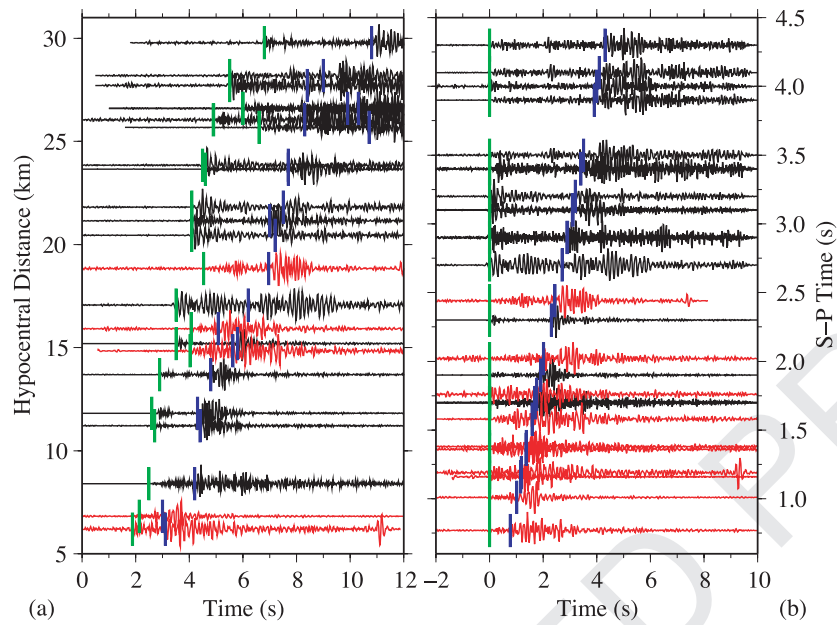
Figure 9. (a) 5 Hz high-pass-filtered seismograms of 5 located triggered (red) and 18 nearby (within 30 km) background (black) events recorded at station NKY. Seismograms are aligned by hypocentral distance from station NKY. Zero time is the event origin time. Green and blue vertical bars show the *P*- and *S*-arrival times, respectively. (b) 5 Hz high-pass-filtered seismograms aligned by the difference in *P*- and *S*-arrival times of 11 triggered (red) and 18 nearby (within 30 km) background (black) events recorded at station NKY. Zero time is the *P*-arrival time. Only the waveforms for the located five events are plotted in (a), while the waveforms for all 11 triggered events at NKY are plotted in (b).
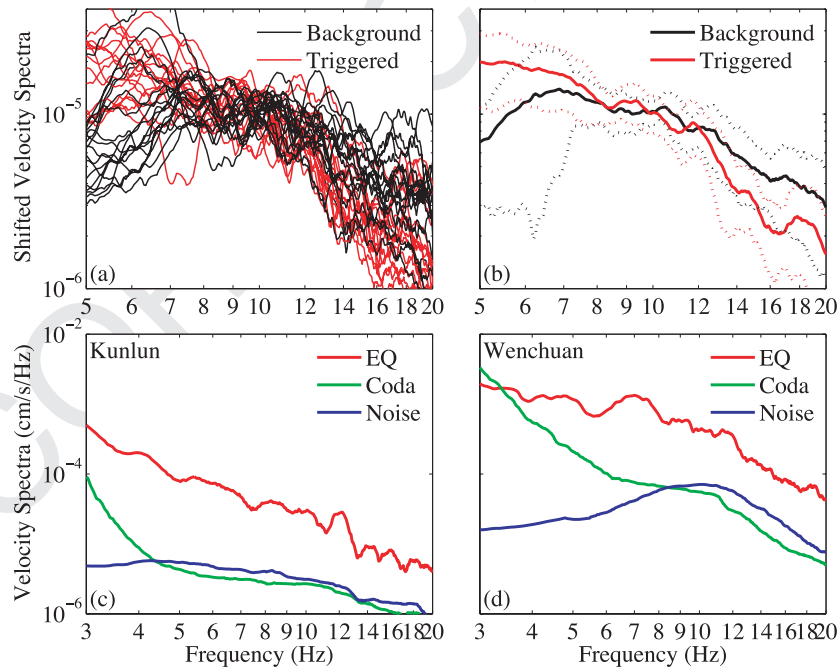

Figure 10. (a and b) Comparison of the shifted velocity spectra of the 15 triggered events (red solid line) and 18 nearby (within 30 km) background events (black solid line). The spectra are computed from the whole waveform including both *P* and *S* waves. (a) Individual spectra of the triggered events (red) and the background events (black). The original velocity spectra are smoothed with half width of 1 Hz to remove the noisy spikes, and then shifted to the same level at the frequency range of 8–12 Hz for comparison of frequency content. (b) Stacked spectra of the triggered events (red solid line) and the background events (black solid line). The red and black dotted lines show the standard deviation for the spectra of triggered and background events, respectively. (c) Comparison of velocity spectra of triggered event (red), teleseismic coda (green), and background noise (blue) for the 2001 Kunlun earthquake. (d) Similar plot as (c) for the 2008 Wenchuan earthquake.

a few percent for large nearby earthquakes (Vidale & Li 2003; Rubinstein & Beroza 2004; Peng & Ben-Zion 2006; Chao & Peng 2009). For teleseismic earthquakes, the velocity reduction could be on the order of 0.2 per cent or even smaller (Zhao *et al.* 2010). This would translate into only a few tens of meters in depth uncertainty at most. In addition, we have examined the *S*-*P* times of the triggered earthquakes and found that they are generally smaller than those of the background earthquakes (Fig. 9).
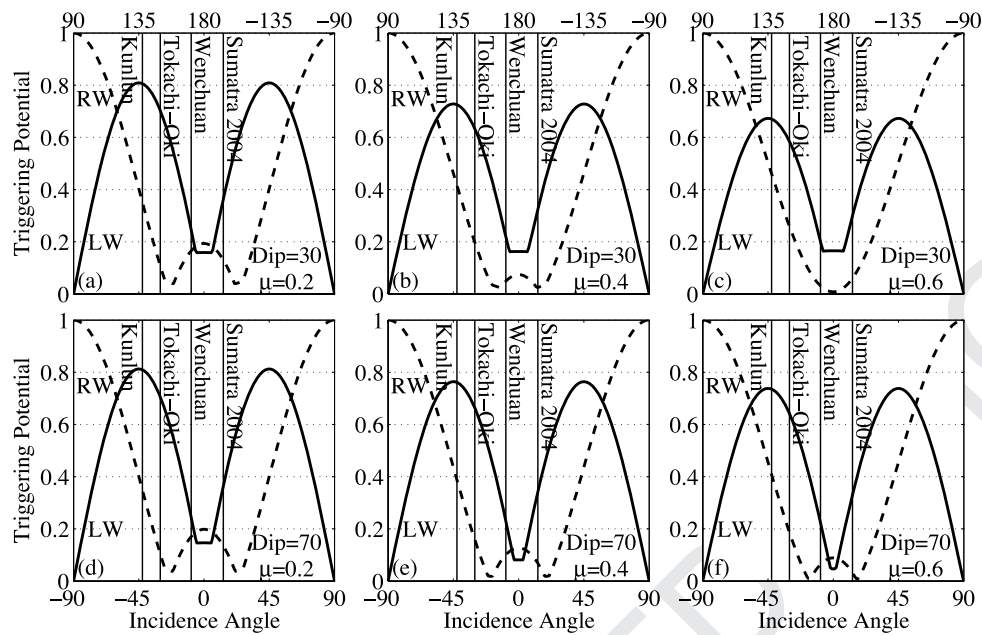
Figure 11. (a) Normalized Love (solid curve) and Rayleigh (dashed curve) wave triggering potential at depth of 4 km on a normal fault dipping at 30° assuming the coefficient of friction $\mu = 0.2$ and comparable displacement amplitudes at the surface for both types of surface waves. Incidence angle is measured counter-clockwise from the fault strike direction (NW). The vertical solid lines show the incidence angle of the four large teleseismic earthquakes utilized in this study. (b) and (c) Similar plot as (a) for $\mu = 0.4$ and 0.6, respectively. (d)–(f) Similar plots as (a)–(c) for a normal fault dipping at 70°, and $\mu = 0.2, 0.4$ and 0.6, respectively.

As briefly mentioned before, the waveforms of the triggered earthquakes do not correlate with those of the background seismicity, indicating that these shallow earthquakes may not occur if they were not triggered. In other words, these events, which are likely located near the velocity strengthening regions in the shallow crust (Wang 2004), are normally aseismic and can only be driven into brittle failure by relatively large dynamic stresses of few tens of KPa or larger (Wang *et al.* 2011; Fischer & Sammis 2009). Such interpretation is also consistent with the fact that the observed spectra of the triggered earthquakes have faster decays at high frequency ranges than those for the nearby background earthquakes (Fig. 10), an indicative of slow earthquakes in the shallow crust (Peng & Gomberg 2010, and references therein). However, the path effects during wave propagation, especially the apparent fast decay due to the lower Q in the shallow crust, could also modify the frequency content of the spectra. We cannot completely rule out the path and other effects at this stage because there is no background seismicity at the immediate vicinity of the triggered earthquakes. This will be addressed in future work when additional information and data become available.

As noted before, these shallow triggered earthquakes appear to be in phase with the passing surface waves (Fig. 7), similar to the recent observations of triggered deep tremor (e.g. Rubinstein *et al.* 2007, 2009; Peng & Chao 2008; Peng *et al.* 2008, 2009; Miyazawa & Brodsky 2008; Miyazawa *et al.* 2008; Gomberg *et al.* 2008; Ghosh *et al.* 2009) and low-frequency earthquakes (Tang *et al.* 2010; Peng *et al.* 2010a). Together with their shallow depths and low frequency contents, we infer that these triggered earthquakes may occur near the transition zone between the velocity strengthening and weakening zones in the top few kilometres of the fault (Wang 2004), which could be considered as the counterpart of the deep tremor and slow-slip events that occurred below the seismogenic zone in the lower crust. We note that the shallow portion of the Babaoshan fault is currently creeping (Che *et al.* 1997; Che & Fan 2003). In addition, clear strain steps have been observed in the nearby borehole strain meters during the 2004 Sumatra and 2008 Wenchuan earthquakes (Aifu Niu, personal communication), and other places in north China during the 2001 M_w 7.8 Kunlun earthquake (Qiu & Shi 2004). We hypothesize that the passing surface waves of the teleseismic earthquakes may trigger micro slow-slip events (Shelly *et al.* 2011) in the shallow portion of the creeping faults, which generate the transient strain step observed in the strain meters. This aseismic motion triggers more rapid slip on scattered regions of the fault that radiate seismic waves (Peng & Gomberg 2010) that are observed on the broadband high-gain seismometers as triggered earthquakes. An alternative hypothesis is that the triggered earthquakes are large and shallow enough to produce the observed strain signals. These hypotheses can be tested by an integrative analysis of the borehole strain meters and seismometers.

Finally, it is worth noting that the modelling of the triggering potential and some discussions are based on the assumption that the triggered earthquakes occur on the NW-striking normal faults. However, these earthquakes also appear to be around the Fangshan Pluton (Fig. 1). Because of the uncertainties in the subsurface structures in this region, the host of the triggered earthquakes is still not clear at this stage. We are in the process of carrying out a dense seismic deployment around this region to improve earthquake locations and better understand the subsurface fault structures. The results from this ongoing deployment will be reported in subsequent publications.

ACKNOWLEDGMENTS

REFERENCES

Brodsky, E., Karakostas, V. & Kanamori, H., 2000. A new observation of dynamically triggered regional seismicity: earthquakes in Greece following the August, 1999 Izmit, Turkey earthquake, *Geophys. Res. Lett.,* **27,** 2741–2744.

Brodsky, E. & Prejean, S., 2005. New constraints on mechanisms of remotely triggered seismicity at Long Valley Caldera, *J. geophys. Res.,* **110,** B04302, doi:04310.01029/02004JB003211.

Brodsky, E., Roeloffs, E., Woodcock, D., Gall, I. & Manga, M., 2003. A mechanism for sustained groundwater pressure changes induced by distant earthquakes, *J. geophys. Res.,* **108,** B8, doi:10.1029/2002JB002321.

Brodsky, E., Sturtevant, B. & Kanamori, H., 1998. Earthquakes, volcanoes, and rectified diffusion, *J. geophys. Res.,* **103,** 23,827–823,838.

Chao, K. & Peng, Z., 2009. Temporal changes of seismic velocity and anisotropy in the shallow crust induced by the 1999 October 22 M6. 4 Chia-Yi, Taiwan earthquake, *Geophys. J. Int.,* **179,** 1800–1816.

Chao, K., Peng, Z., Wu, C., Tang, C.-C. & Lin, C.H., 2011. Remote triggering of non-volcanic tremor around Taiwan, *Geophys. J. Int.,* in review.

Che, Z. & Fan, Y., 2003. Tracing study of fault activity of the Beijing Huangzhuang-Gaoliying fault and Babaoshan fault in recent time, *Earthquake,* **23,** 97–104.

Che, Z., Gong, Y., Liu, S., Liu, T. & Meng, G., 1997. Comprehensive study of fault activity of the Huangzhuang-Gaoliying and Babaoshan Fault in the middle section, *Earthq. Res. China,* **13,** 330–337.

Chen, L., Tao, W., Zhao, L. & Zheng, T., 2008. Distinct lateral variation of lithospheric thickness in the Northeastern North China Craton, *Earth planet. Sci. Lett.,* **267,** 56–68.

Chen, Q., Chen, Y. & Li, L., 2006. China digital seismic network improves coverage and quality, *EOS, Trans. Am. geophys. Un.,* **87,** doi:10.1029/2006EO300003.

Deng, Q., Zhang, P., Ran, Y., Yang, X., Min, W. & Chu, Q., 2003. Basic characteristics of active tectonics of China, *Sci. China Ser. D: Earth Sci.,* **46,** 356–372.

Fischer, A. & Sammis, C., 2009. Dynamic driving of small shallow events during strong motion, *Bull. seism. Soc. Am.,* **99,** 1720.

Freed, A., 2005. Earthquake triggering by static, dynamic, and postseismic stress transfer, *Annu. Rev. Earth planet. Sci,* **33,** 335–367.

Ghosh, A., Vidale, J., Peng, Z., Creager, K. & Houston, H., 2009. Complex non-volcanic tremor near Parkfield, California, triggered by the great 2004 Sumatra earthquake, *J. geophys. Res,* **114,** B00A15, doi:10.1029/2008JB006062.

Gomberg, J., Blanpied, M. & Beeler, N., 1997. Transient triggering of near and distant earthquakes, *Bull. seism. Soc. Am.,* **87,** 294–309.

Gomberg, J., Bodin, P., Larson, K. & Dragert, H., 2004. Earthquakes nucleated by transient deformations fundamental process evident in observations surrounding the M7. 9 Denali Fault Alaska Earthquake, *Nature,* **427,** 621–624.

Gomberg, J., Reasenberg, P., Bodin, P. & Harris, R., 2001. Earthquake triggering by seismic waves following the Landers and Hector Mine earthquakes, *Nature,* **411,** 462–466.

Gomberg, J., Reasenberg, P., Cocco, M. & Belardinelli, M., 2005. A frictional population model of seismicity rate change, *J. geophys. Res.,* **110,** B05S03, doi:10.1029/2004JB003404.

Gomberg, J., Rubinstein, J., Peng, Z., Creager, K., Vidale, J. & Bodin, P., 2008. Widespread triggering of nonvolcanic tremor in California, *Science,* **319,** 173.

Gonzalaz-Huizar, H. & Velasco, A., 2010. Dynamic triggering: stress modeling and a case study, in review.

Hill, D., 2008. Dynamic stresses, Coulomb failure, and remote triggering, *Bull. seism. Soc. Am.,* **98,** 66–92.

Hill, D., 2010. Surface wave potential for triggering tectonic (non-volcanic) tremor, *Bull. seism. Soc. Am.,* **100,** 1859–1878.

Hill, D., Pollitz, F. & Newhall, C., 2002. Earthquake-volcano interactions, *Phys. Today,* **55,** 41–47.

Hill, D. & Prejean, S., 2007. Dynamic triggering, in *Earthquake Seismology Treatise on Geophysics,* pp. 257–291, ed. Kanamori, H.

Hill, D., Reasenberg, P., Michael, A., Arabaz, W., Beroza, G., Brumbaugh, D., Brune, J., Castro, R., Davis, S. & DePolo, D., 1993. Seismicity remotely triggered by the magnitude 7.3 Landers, California, earthquake, *Science,* **260,** 1617–1623.

Hough, S., 2005. Remotely Triggered Earthquakes Following Moderate Mainshocks (or, Why California Is Not Falling into the Ocean), *Seism. Res. Lett.,* **76,** 58–66.

Hough, S. & Kanamori, H., 2002. Source properties of earthquakes near the Salton Sea triggered by the 16 October 1999 M 7.1 Hector Mine, California, earthquake, *Bull. seism. Soc. Am.,* **92,** 1281–1289.

Hough, S., Seeber, L. & Armbruster, J., 2003. Intraplate triggered earthquakes: observations and interpretation, *Bull. seism. Soc. Am.,* **93,** 2212–2221.

Jiang, T., Peng, Z., Wang, W.J. & Chen, Q.F., 2010. Remotely triggered seismicity in Continental China by the 2008 M_w 7.9 Wenchuan earthquake, *Bull. seism. Soc. Am.,* **100**(5B), 5274–5289, doi:5210.1785/0120090286.

Johnson, P. & Jia, X., 2005. Nonlinear dynamics, granular media and dynamic earthquake triggering, *Nature,* **7060,** 871.

Johnston, M., Prejean, S. & Hill, D., 2004. Triggered deformation and seismic activity under Mammoth mountain in Long Valley Caldera by the 3 November 2002 M_w 7.9 Denali Fault earthquake, *Bull. seism. Soc. Am.,* **94,** S360–S369.

Kilb, D., Gomberg, J. & Bodin, P., 2002. Aftershock triggering by complete Coulomb stress changes, *J. geophys. Res.,* **107,** B4, doi:10.1029/2001JB000202.

Klein, F., 2002. User's guide to HYPOINVERSE-2000, a Fortran program to solve for earthquake locations and magnitudes, *US Geol. Surv. Open-File Rept,* 02–171.

Liang, S., Li, Y., Shu, P. & Zhu, P., 2008. On the determinng of source parameters of small earthquakes by using amplitude ratios of P and S from regional network observations, *Acta Seismol. Sin.,* **27,** 249–257.

Linde, A. & Sacks, I., 1998. Triggering of volcanic eruptions, *Nature,* **395,** 888–890.

Liu, R., Wu, Z., Yin, C., Chen, Y. & Zhuang, C., 2003. Development of China digital seismological observational systems, *Acta Seismol. Sin.,* **16,** 568–573.

Matthews, M. & Reasenberg, P., 1988. Statistical methods for investigating quiescence and other temporal seismicity patterns, *Pure appl. Geophys.,* **126,** 357–372.

Miyazawa, M. & Brodsky, E., 2008. Deep low-frequency tremor that correlates with passing surface waves, *J. geophys. Res.,* **113,** B01307, doi:01310.01029/02006JB004890.

Miyazawa, M., Brodsky, E. & Mori, J., 2008. Learning from dynamic triggering of low-frequency tremor in subduction zones, *Earth Planets Space,* **60,** e17–e20.

Miyazawa, M. & Mori, J., 2006. Evidence suggesting fluid flow beneath Japan due to periodic seismic triggering from the 2004 Sumatra-Andaman earthquake, *Geophys. Res. Lett.,* **33,** L05303.

Pankow, K., Arabasz, W., Pechmann, J. & Nava, S., 2004. Triggered seismicity in Utah from the 3 November 2002 Denali fault earthquake, *Bull. seism. Soc. Am.,* **94,** S332–S347.

Peng, Z. & Ben-Zion, Y., 2006. Temporal Changes of Shallow Seismic Velocity Around the Karadere-Düzce Branch of the North Anatolian Fault and Strong Ground Motion, *Pure appl. Geophys.,* **163,** 567–600.

Peng, Z. & Chao, K., 2008. Non-volcanic tremor beneath the Central Range in Taiwan triggered by the 2001 M_w 7.8 Kunlun earthquake, *Geophys. J.Int.,* **175,** 825–829.

Peng, Z. & Gomberg, J., 2010. An integrative perspective of coupled seismic and aseismic slow slip phenomena, *Nat. Geosci.,* doi:10.1038/ngeo1940.

Peng, Z., Hill, D.P., Shelly, D.R. & Aiken, C., 2010a. Remotely triggered microearthquakes and tremor in Central California following the 2010 M_w 8.8 Chile Earthquake, *Geophys. Res. Lett.,* doi:10.1029/2010GL045462, in press.

Peng, Z., Long, L.T. & Zhao, P., 2011. The relevance of high-frequency analysis artifacts to remote triggering, *Bull. seism. Soc. Am.,* in review.

Q9 Peng, Z., Vidale, J., Creager, K., Rubinstein, J., Gomberg, J. & Bodin, P., 2008. Strong tremor near Parkfield, CA, excited by the 2002 Denali Fault earthquake, *Geophys. Res. Lett.,* **35,** L23305, doi:23310.21029/22008GL036080.

Peng, Z., Vidale, J., Wech, A., Nadeau, R. & Creager, K., 2009. Remote triggering of tremor along the San Andreas Fault in central California, *J. geophys. Res,* **114,** B00A06, doi:10.1029/2008JB006049.

Peng, Z., Wang, W.J., Chen, Q.F. & Jiang, T., 2010b. Remotely triggered seismicity in north China following the 2008 M_w 7.9 Wenchuan earthquake, *Earth Planets Space,* **62,** 893–898.

Perfettini, H., Schmittbuhl, J. & Cochard, A., 2003. Shear and normal load perturbations on a two-dimensional continuous fault: 2. Dynamic triggering, *J. geophys. Res,* **108,** B9, 2409, doi:2410.1029/2002JB001805.

Prejean, S. *et al.*, 2004. Remotely triggered seismicity on the United States west coast following the M_w 7.9 Denali Fault earthquake, *Bull. seism. Soc. Am.,* **94,** S348–S359.

Qiu, Z. & Shi, Y., 2004. Application of observed strain steps to the study of remote earthquake stress triggering, *Acta Seismol. Sin.,* **17,** 534–541.

Reasenberg, P. & Simpson, R., 1992. Response of regional seismicity to the static stress change produced by the Loma Prieta earthquake, *Science,* **255,** 1687–1690.

Rubinstein, J. & Beroza, G., 2004. Evidence for Widespread Nonlinear Strong Ground Motion in the M_w 6.9 Loma Prieta Earthquake, *Bull. seism. Soc. Am.,* **94,** 1595–1608.

Rubinstein, J., Gomberg, J., Vidale, J., Wech, A., Kao, H., Creager, K. & Rogers, G., 2009. Seismic wave triggering of nonvolcanic tremor, episodic tremor and slip, and earthquakes on Vancouver Island, *J. geophys. Res.,* **114,** B00A01, doi:10.1029/2008JB005875.

Rubinstein, J., Vidale, J., Gomberg, J., Bodin, P., Creager, K. & Malone, S., 2007. Non-volcanic tremor driven by large transient shear stresses, *Nature,* **448,** 579–582.

Shelly, D., Beroza, G., Ide, S. & Nakamula, S., 2006. Low-frequency earthquakes in Shikoku, Japan, and their relationship to episodic tremor and slip, *Nature,* **442,** 188–191.

Shelly, D., Peng, Z., Hill, D.P. & Aiken, C., 2011. Tremor evidence for dynamically triggered creep events on the deep San Andreas Fault, *Nat. Geosci.,* in review.

Q10 Stein, S. & Wysession, M., 2003. *An Introduction to Seismology, Earthquakes, and Earth Structure,* pp. 88–90, Blackwell Publishing, Malden, MA, USA.

Tang, C.-C., Peng, Z., Chao, K., Chen, C.-H. & Lin, C.-H., 2010. Detecting low-frequency earthquakes within non-volcanic tremor in Southern Taiwan triggered by the 2005 M_w 8.6 Nias Earthquake, *Geophys. Res. Lett.,* **37,** L16307, doi:16310.11029/12010GL043918.

Van Der Elst, N. & Brodsky, E., 2010. Connecting near-field and far-field earthquake triggering to dynamic strain, *J. geophys. Res.,* **115,** B07311, doi:07310.01029/02009JB006681.

Velasco, A., Hernandez, S., Parsons, T. & Pankow, K., 2008. Global ubiquity of dynamic earthquake triggering, *Nat.Geosci.,* **1,** 375–379.

Vidale, J. & Li, Y., 2003. Damage to the shallow Landers fault from the nearby Hector Mine earthquake, *Nature,* **421,** 524–526.

Waldhauser, F., 2001. HypoDD-A program to compute double-difference hypocenter locations, *US Geological Survey. Open File Report*, 01–113.

Wang, J., 2004. Technique Study of across-fault deformation Measurement and its application, *Chin. J. Rock Mech. Engg.,* **23,** 261–266.

Wang, Y., Zhou, L. & Li, J., 2011. Intracontinental superimposed tectonics—A case study in the Western Hills of Beijing, eastern China, *Geol. Soc. Am. Bull.,* doi:10.1130/B30257.30251.

Yan, D., Zhou, M., Song, H., Wang, G. & Sun, M., 2006. Mesozoic extensional structures of the Fangshan tectonic dome and their subsequent reworking during collisional accretion of the North China Block, *J. Geol. Soc.,* **163,** 127–142.

Zhao, P., Peng, Z. & Sabra, K., 2010. Detecting remotely triggered temporal changes around the Parkfield section of the San Andreas Fault, *Earthq. Sci.,* **23,** 497–509.

APPENDIX A: β STATISTICS

The β statistics measures the differences between the observed number of events after the main shock and the expected number from the average seismicity rate before the main shock, and is scaled by the standard deviation of the seismicity rate (Matthews & Reasenberg 1988; Reasenberg & Simpson 1992). It is defined by

$$\beta(n_a, n_b; t_a, t_b) = \frac{n_a - E(n_a)}{\mathrm{Var}(n_a)}, \tag{A1}$$

where n_b and n_a are the number of earthquakes observed before and after the main shock, t_b and t_a are the time duration before and after the main shock, respectively. $E(n_a)$ is the expected number of events within the period t_a and $\mathrm{Var}(n_a)$ is the standard deviation. For a binomial process, $E(n_a) = n_b(t_a/t_b)$, and $\mathrm{Var}(n_a) = n_b(t_a/t_b)(1 - n_b/n_a)$ (Gomberg *et al.* 2001; Kilb *et al.* 2002; Pankow *et al.* 2004; Hough 2005). When the seismicity rate before the main shock is small enough, the binomial process could be simplified as a Poisson process, where $E(n_a) = \mathrm{Var}(n_a) = n_b(t_a/t_b)$ (Hill & Prejean 2007). Results with $|\beta| > 2$ (approximately two standard deviations) are generally considered as statistically significant (Reasenberg & Simpson 1992; Hill & Prejean 2007).

Next, we manually pick earthquakes on the high-pass filtered seismograms 6 hr before and 1 hr after the *P* arrival of each teleseismic event for station BJT. We first take the envelope function of the 5 Hz high-pass filtered seismogram, smooth it with half window width of 1 Hz, and stack the resulting three-component envelopes to obtain the envelope function for each event-station pair. Next, we identify the events by searching for clear double peaks in the envelope function that correspond to *P* and *S* waves. We use 10 times of the median absolute deviation (MAD) with duration of 1 hr before the *P* arrival as amplitude threshold. Only the events with amplitude larger than the threshold are used to compute the β statistics to ensure that the handpicked events are not caused by the random fluctuations or near-surface high frequency noises. Finally, we replace the number of earthquakes n_b and n_a with the amplitude-normalized number of N_b and N_a that are defined by $N_b = n_b$ and $N_a = n_b \sum_{i=1}^{n_a} A_i' / \sum_{i=1}^{n_b} A_i$, where A_i and A_i' are the amplitudes of events before and after the main shock (Miyazawa & Mori 2006; Jiang *et al.* 2010). When there is no earthquake before the main shock, we assume $N_b = n_b = 0.25$, and $\frac{1}{n_b}\sum_{i=1}^{n_b} A_i = 10 \times \mathrm{MAD}$ to compute N_a following Kilb *et al.* (2002) and Jiang *et al.* (2010).

For the β statistics for all the CC stations, t_a and t_b depend on the length of available seismic data. For the β statistics based on regional catalogue, we infer the scaled amplitude of the each event from the magnitude using a simple scaling relationship $A = \sqrt{10^{M_w}}$ (Stein & Wysession 2003), where A and M_w are the scaled amplitude and moment magnitude, respectively.

APPENDIX B: TRIGGERING POTENTIAL MODELLING

For a right-hand coordinate system x_i where $i = 1, 2, 3$, with the vertical axis (x_3) positive with depth, the displacements for the Rayleigh waves propagating in the x_1 direction are only in x_1 and x_3 directions (Stein & Wysession 2003)

$$u_1 = A_R k_1 \sin(\omega t - k_1 x) [\exp(-0.85 k_1 z) - 0.58 \exp(-0.39 k_1 z)] \tag{B1}$$

$$u_3 = A_R k_1 \cos(\omega t - k_1 x) \times [-0.85 \exp(-0.85 k_1 z) + 1.47 \exp(-0.39 k_1 z)], \tag{B2}$$

where A_R is the amplitude of the Rayleigh wave, ω is the angular frequency, k_1 is the horizontal wave number, and x_3 is the depth. The displacements for Love wave within a layer (thickness $H = 35$ km) over a half-space is only in the x_2 direction (Stein & Wysession 2003)

$$u_2 = A_L \exp\left[\mathrm{i}\left(\omega t - k_1 x_1\right)\right] \cos\left(k_1 x_3 \sqrt{c_1^2/\beta_1^2 - 1}\right), \tag{B3}$$

where A_L is the amplitude of the Love wave, c_1 is the horizontal apparent velocity, and β_1 is the shear wave velocity within the top layer. For both the Rayleigh and Love waves, the strains induced by the displacements are (Stein & Wysession 2003)

$$\varepsilon_{ij} = \varepsilon_{ji} = \frac{1}{2}(u_{i,j} + u_{j,i}), \tag{B4}$$

where $u_{i,j}$ is the first derivative of the displacement in the x_i direction relative to the x_j direction. For Poisson solid, the dynamic stresses (compression as negative) caused by the Rayleigh waves are (Gonzalaz-Huizar & Velasco 2010)

$$\sigma_{ii} = \lambda(3\varepsilon_{ii} + \varepsilon_{jj}) \tag{B5}$$

$$\sigma_{ij} = 2\lambda\varepsilon_{ij}, \tag{B6}$$

where λ is the Lamé constant, and $i = 1, j = 3$, or $i = 3, j = 1$, because Rayleigh wave propagating in x_1 direction do not introduce motion in the x_2 direction. The dynamic stresses caused by the Love waves are (Gonzalaz-Huizar & Velasco 2010)

$$\sigma_{ij} = \sigma_{ji} = 2G\varepsilon_{ij}, \tag{B7}$$

where G is the shear modulus, and $i = 1, j = 2$, or $i = 3, j = 2$, because Love wave propagating in x_1 direction only introduce shear stresses in x_2 direction. Using eqs. (A1) and (B1)–(B6), we model the dynamic stresses as a function of the wave incident angle, depth, and time, and then rotate the dynamic stresses σ_{ij} in coordinate system x_i to σ_{kl} in a new coordinate system y_i, where y_1, y_2, y_3, are the fault strike, fault dip, and fault plane normal directions, respectively, using two unitary matrices

$$UM_1 = \begin{bmatrix} \cos(\theta) & \sin(\theta) & 0 \\ -\sin(\theta) & \cos(\theta) & 0 \\ 0 & 0 & 1 \end{bmatrix} \tag{B8}$$

$$UM_2 = \begin{bmatrix} 1 & 0 & 0 \\ 0 & \cos(\delta) & -\sin(\delta) \\ 0 & \sin(\delta) & \cos(\delta) \end{bmatrix} \tag{B9}$$

$$\sigma_{kl} = (UM_1 UM_2)^T \sigma_{ij} (UM_1 UM_2), \tag{B10}$$

where θ and δ are the incident angles of the seismic waves and fault dip angle, respectively.

Finally, we compute the triggering potential of a incident Rayleigh or Love wave, as the change in Coulomb failure function (Hill 2010)

$$\Delta CCF = \tau + \mu\sigma_n, \tag{B11}$$

where τ is the dynamic shear stress, σ_n is the dynamic normal stress acting on the fault plane, and μ is the friction coefficient. In our case, the triggered fault is likely to be normal as mentioned in Section 2.1, so the triggering potential is defined as (Gonzalaz-Huizar & Velasco 2010)

$$P_N = -\tau_d + \mu\sigma_n, \tag{B12}$$

where τ_d is dynamic shear stress in the fault dip direction.

The model parameters we employed are $\lambda = G = 3 \times 10^{10}$ Pa, $\mu = 0.2, 0.4$ or 0.6, $f = 0.05$ Hz, $c_1 = 3.78$ km s^{-1}, $\beta_1 = 3.5$ km s^{-1} (Hill 2010), $\delta = 30°$ (for Babaoshan fault) or $70°$ (for Huangzhuang-Gaoliying fault). The output is the triggering potential as a function of wave incident angle θ from 0 to $360°$, depth from 0 to 30 km and time from 0 to 30 s for a normal fault.

SUPPORTING INFORMATION

Additional Supporting Information may be found in the online version of this article:

Table S1. List of the information for all the 39 teleseismic events recorded by the station BJT utilized in this study and some computed parameters. Fields 1 to 19 are: event ID, year, day of year, hour, minute, second, latitude, longitude, depth (km), magnitude (M_w), distance to BJT (km), back azimuth (degree), Transient PGV (cm s^{-1}), radial PGV (cm s^{-1}), vertical PGV (cm s^{-1}), triggering quality (0 for no clear signal, 1 for Rayleigh waves, 2 for Love waves, 3 for S waves, 4 for P waves and five for multiple phases), β value, and comments.
Table S2. List of the information for all the 19 triggered events found in this study. Fields 1 to 10 are: year, name of large teleseismic event, station, hand-picked P-arrival time (s), hand-picked S-arrival time (s), longitude, latitude, depth (km), local magnitude (M_L) and event ID of the triggered event.

Please note: Wiley-Blackwell are not responsible for the content or functionality of any supporting materials supplied by the authors. Any queries (other than missing material) should be directed to the corresponding author for the article.